Nanoscale

PAPER

View Article Online
View Journal | View Issue

Cite this: *Nanoscale*, 2024, **16**, 12550

Efficient reduction of CO_2 and inhibition of hydrogen precipitation by polyoxometalate photocatalyst modified with the metal Mn†

Guifen Li,[a] Yulan Gu,[a] Rui Ren,[a] Sitan Li,*[a] Houen Zhu,[a] Dongdong Xue,[a] Xiangyi Kong,[a] Ziyi Zheng,[a] Nuo Liu,[a] Bei Li*[b] and Jiangwei Zhang *[a,c]

Received 8th January 2024,
Accepted 29th April 2024

DOI: 10.1039/d4nr00097h

rsc.li/nanoscale

Photocatalytic reduction of CO_2 to chemical fuels is attractive for solving both the greenhouse effect and the energy crisis, but the key challenge is to design and synthesize photocatalysts with remarkable performance under visible light irradiation. Efficient catalytic carbon dioxide reduction (CO_2RR) with light is considered a promising sustainable and clean approach to solve environmental problems. Herein, we found a new photocatalyst ($[Mn(en)_2]_6[V_{12}B_{18}O_{54}(OH)_6]$) (abbreviated as Mn_6V_{12}) based on the modifiability of polyoxometalates, in which Mn acts as a modifying unit to efficiently reduce CO_2 to CO and effectively inhibit the hydrogen precipitation reaction. This Mn modified polyoxometalate catalyst has a maximum CO generation rate of 4625.0 μmol g^{-1} h^{-1} and a maximum H_2 generation rate of 499.6 μmol g^{-1} h^{-1}, with a selectivity of 90.3% for CO generation and 9.7% for H_2 generation. This polyoxometalate photocatalyst can effectively reduce CO and inhibit the hydrogen precipitation reaction. It provides a new idea for the efficient photocatalytic carbon dioxide reduction (CO_2RR) with polyoxometalate catalysts.

1. Introduction

With the burning of large quantities of carbon containing fossil fuels and the anthropogenic emission of CO_2 into the atmosphere, the problem of global warming is worsening, threatening the safety of human society and the natural living environment.[1] The environmental problems brought about by the greenhouse effect, energy shortages and fossil energy consumption have become major challenges for the common future of mankind.[2–4] Therefore, Carbon Capture, Utilization and Storage (CCUS) is considered to be one of the most realistic ways to mitigate CO_2 concentration and slow down global warming.[5,6] Among various CO_2 utilization technologies, the conversion of CO_2 into chemicals and fuels through solar photocatalysis holds great promise for solving the global energy shortage and reducing the greenhouse effect.[7,8] The reduction of CO_2 to valuable hydrocarbon fuels also offers a promising strategy for a carbon neutrality energy cycle.[9] The conversion of CO_2 into commercial chemicals and useful fuels, similar to that of plant photosynthesis by modelling plant photosynthesis, has a wide range of applications in the organic industry and in oxidation fuel cells.[10–17] This slows down energy consumption processes and reduces CO_2 concentrations.[18,19] The two-electron reduction products of syngas (from CO and H_2) and formic acid are important raw materials and liquid fuels that are widely recognized as promising renewable fuels, which are also highly conducive to alleviating the energy crisis and climate change.[20–22]

Polyoxometalates (POMs) are a class of clusters formed by the coordination of early transition metals such as Mo, W, V, *etc.* in their highest oxidation states with oxygen atoms.[23–26] Which is an inorganic crystalline material with an oxygen-rich surface that has excellent physical and chemical properties.[27] It has been extensively studied in the fields of catalysis, medicine and materials science.[28,29] POMs can not only be structurally modified at the molecular level, but also have a good ability to carry and release electrons without changing their structural properties.[30] Driven by light, electrons in POMs can be excited from the highest occupied molecular orbital (HOMO) to the lowest unoccupied molecular orbital (LUMO), and the excited electrons are transferred from the valence band (VB) to the conduction band (CB) between the valence bands, resulting in the formation of electron–hole pairs in the valence and conduction bands, and the electron–hole pairs

[a]*College of Energy Material and Chemistry, Inner Mongolia University, Hohhot 010021, P. R. China. E-mail: sitanli@imu.edu.cn, zjw11@tsinghua.org.cn, jwz@imu.edu.cn*
[b]*Cancer Centre and Institute of Translational Medicine, Faculty of Health Sciences, MoE Frontiers Science Center for Precision Oncology, University of Macau, Macau SAR 999078, China. E-mail: beili@um.edu.mo*
[c]*Ordos Laboratory, Ordos 017000, P. R. China*

†Electronic supplementary information (ESI) available. CCDC 2324078. For ESI and crystallographic data in CIF or other electronic format see DOI: https://doi.org/10.1039/d4nr00097h

have a strong redox property and are used to catalyze the redox reactions.[31,32] These advantages give POMs unique properties for photocatalytic CO_2 reduction. In addition, the modifiability of the structure facilitates the introduction of functional groups and transition metals as active center to modulate the yield and selectivity of CO_2 reduction.[33] Transition metal modified polyoxometalates with redox pairs facilitate electron transfer and indicate structure–activity relationships in photochemical CO_2 reduction, exhibiting good photocatalytic activity for CO_2 reduction for more efficient solar-to-chemical energy conversion.[34,35] As a result, more and more attention has been paid to the potential applications in various fields. However, currently developed catalysts for photocatalytic CO_2 reduction still suffer from a number of limitations, including restricted use of visible light and poor selectivity.[7] Therefore, it is urgent and challenging to explore new transition metal modified polyoxometalate photocatalysts with high activity and selectivity.

In this paper, we present a new vanadium borate cluster based on modification with the metal Mn,[36–38] ([Mn$(en)_2]_6[V_{12}B_{18}O_{54}(OH)_6$]) (abbreviated as Mn_6V_{12}) can reduce CO_2 to CO with high efficiency and inhibit the hydrogen precipitation reaction effectively. The Mn modified vanadium borate clusters showed a maximum CO production rate of 4625.0 μmol g^{-1} h^{-1} and a maximum H_2 production rate of 499.6 μmol g^{-1} h^{-1}, with a selectivity of 90.3% for CO production and 9.7% for H_2 production. The high efficiency of CO reduction and the effective inhibition of hydrogen precipitation reaction were better than those of the same type of polyoxometalate catalysts. It provides a new way for the efficient photocatalytic carbon dioxide reduction (CO_2RR) of transition metal modified polyoxometalate photocatalysts.

Jiangwei Zhang

Prof. Dr Jiangwei Zhang is currently a "Steed plan High level Talents" Professor, "Grassland Talents" of Inner Mongolia Autonomous Region, Principle Investigator from College of Energy Material and Chemistry under leadership of Dean Academician Dongyuan Zhao, Inner Mongolia University. He received his Ph.D. from the Department of Chemistry, Tsinghua University (THU) in 2016. He has published 184 innovative publications with H-index = 45. Currently, His research focuses on the common key scientific issues "materials structure and reaction mechanism dynamically and precisely by visual detection and determination" and "Advanced characterization methodology and energy catalytic materials – Interdisciplinary".

2. Experimental component

2.1. Synthesis of [Mn$(en)_2]_6[V_{12}B_{18}O_{54}(OH)_6$]

The synthesis was based on known literature and replaced with $Mn(CH_3COO)_2{\cdot}4H_2O$ (0.623 g, 2.5 mmol), other reaction conditions were not changed.[39] Further details on the experimental methods and procedures are described in the ESI.†

2.2. Photocatalytic reactions

Prior to the reduction, 2 mL of triethanolamine (TEOA) was used as a sacrificial reagent, [Ru(bpy)$_3$] $Cl_2{\cdot}6H_2O$ 11.6 mg as a photosensitizer, 8 mL of acetonitrile (CH_3CN) and 2 mL of deionized water as solvents, and they were transferred into a 60 mL quartz glass reactor with a dispersed catalyst (2 mg) with a lid to carry out the photocatalytic reduction of CO_2 experiment. Afterwards, CO_2 gas was bubbled into the mixed solution for 15 min until the CO_2 concentration was saturated and oxygen was removed from the device to ensure that the system was carried out in a CO_2 atmosphere. The reaction was kept at ~20°C by condensing circulating water and irradiated under a 300 W xenon lamp with a 420 nm cut-off filter. After 1 h of illumination under visible light, the gaseous products (CO and H_2) were collected with a 1 mL syringe and then immediately tested and analysed with a GC-2014C.

XAFS measurements. The X-ray absorption find structure spectra V and Mn K-edge data were collected in transmission mode while the corresponding reference and the corresponding oxide reference sample were collected in transmission mode in TableXAFS-500A from Anhui Chuangpu Instrument Technology Co., Ltd. The sample were grinded and uniformly daubed on the special adhesive tape.

XAFS analysis and results. The acquired EXAFS data were processed according to the standard procedures using the ATHENA module of Demeter software packages.

The EXAFS spectra were obtained by subtracting the post-edge background from the overall absorption and then normalizing with respect to the edge-jump step. Subsequently, the $\chi(k)$ data of were Fourier transformed to real (R) space using a hanging windows (dk = 1.0 Å^{-1}) to separate the EXAFS contributions from different coordination shells. To obtain the quantitative structural parameters around central atoms, least-squares curve parameter fitting was performed using the ARTEMIS module of Demeter software packages

The following EXAFS equation was used:

$$\chi(k) = \sum_j \frac{N_j S_0{}^2 F_j(k)}{kR_j{}^2} \cdot \exp[-2k^2\sigma_j{}^2] \cdot \exp\left[\frac{-2R_j}{\lambda(k)}\right] \cdot \sin[2kR_j + \phi_j(k)]$$

the theoretical scattering amplitudes, phase shifts and the photoelectron mean free path for all paths calculated. $S_0{}^2$ is the amplitude reduction factor, $F_j(k)$ is the effective curved-wave backscattering amplitude, N_j is the number of neighbours in the j^{th} atomic shell, R_j is the distance between the X-ray absorbing central atom and the atoms in the j^{th} atomic shell (backscattered), λ is the mean free path in Å, $\phi_j(k)$ is the phase shift (including the phase shift for each shell and the

total central atom phase shift), σ_j is the Debye–Waller parameter of the j^{th} atomic shell (variation of distances around the average R_j). The functions $F_j(k)$, λ and $\phi_j(k)$ were calculated with the *ab initio* code FEFF10. The additional details for EXAFS simulations are given below.

All fits were performed in the R space with k-weight of 2 while phase correction was also applied in the first coordination shell to make R value close to the physical interatomic distance between the absorber and shell scattered. The coordination numbers of model samples were fixed as the nominal values. While the S_0^2, internal atomic distances R, Debye–Waller factor σ^2, and the edge-energy shift Δ were allowed to run freely.

X-ray crystallography. Data collections were performed by BL17B beamline of National Facility for Protein Science (NFPS), Shanghai Synchrotron Radiation Facility (SSRF) Shanghai. Data reduction, cell refinement and experimental absorption correction were performed with the software package of Bruker APEX5. The structures were solved by intrinsic phasing and refined against F^2 by full-matrix least-squares. All non-hydrogen atoms were refined anisotropically. All the calculations were carried out by the program package of SHELX and Olex2 ver 1.2.10.

Crystal data and structure refinement for compound 1. **Compound 1** $[Mn(en)_2]_6[V_{12}B_{18}O_{54}(OH)_6]$: $C_{24}H_{96}B_{18}Mn_6N_{24}O_{60}V_{12}$, trigonal, space group $R\bar{3}$ (No. 148), $a = b = 21.0608$ Å, $c = 21.1268$ Å, $\alpha = \beta = 90°$, $\gamma = 120°$, $V = 8115.5$ Å^3, $Z = 3$, 3176 reflections measured, $R_1 = 0.0640$, w$R_2 = 0.0826$.

CCDC 2324078 contains the supplementary crystallographic data for compound **1** respectively in this paper.†

3. Results and discussion

3.1. Catalyst structure

As shown in Fig. 1a and b, Mn_6V_{12} has a $B_{18}O_{42}$ ring consisting of six B_3O_7 ternary rings sharing oxygen atoms. The top of the ring consists of six VO_5 quadrangular cones conjoined by the common side of the lid, and the bottom is two segments consisting of three VO_5 quadrangular cones conjoined by the common side.[40] Overall there is a V12 cluster embedded in the B18 ring. In the $[B_3O_7]$ unit, the B atom displays two different coordination geometries. Two B atoms are coordinated with four oxygen atoms to form a tetrahedral shape. One B atom is coordinated with three oxygen atoms to form a planar triangle. The oxygen atom on the periphery of the B18 ring is attached to the transition metal Mn and the ring is modified with six manganese ions. From the TEM image of Mn_6V_{12} (Fig. 1c), it is observed that Mn_6V_{12} is similar to spherical micron-sized plush clusters, and the plush edges are a lot of consisting of thin and long rod-like structures with a crystallographic spacing of $d = 0.32$ nm. The extensive rod-like structure is supposed to be the active center of the cluster and serves to increase the active site.

In order to determine the valence and coordination structure of atoms at the atomic level, X-ray absorption fine structure (XAFS) measurements were performed.[41,42] The electronic structures and coordination environments of V and Mn in Mn_6V_{12} were analyzed using X-ray absorption spectroscopy (XAS), as well as Mn foil, MnO, MnO_2, MnPc, V foil, and V_2O_5 as standard references. In Fig. 2a, X-ray measurements in terms of the K-edge of V in the absorption near edge structure

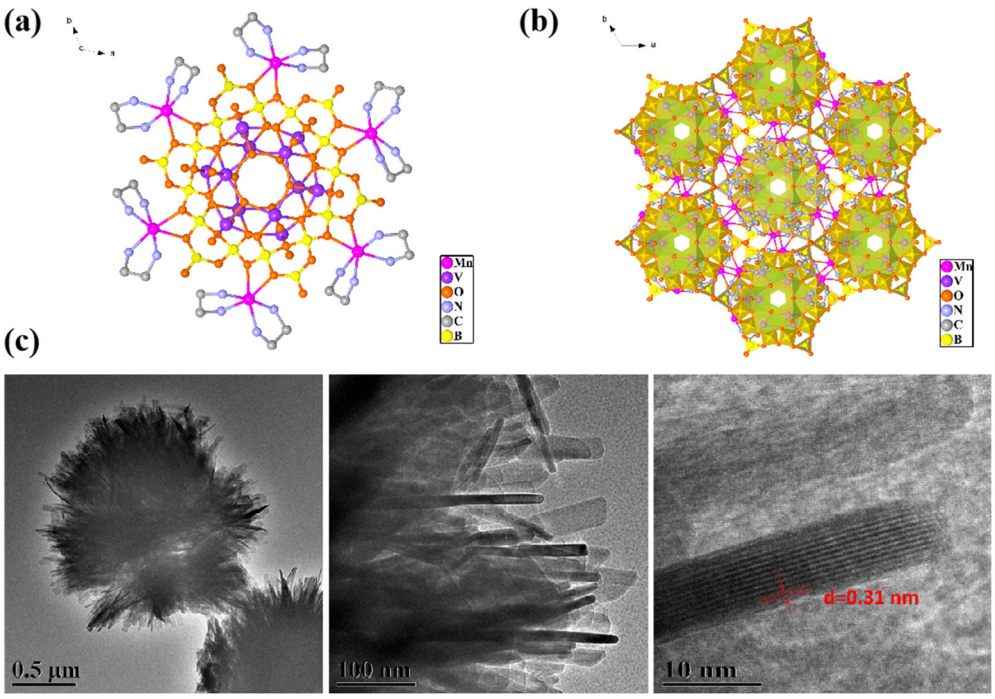

Fig. 1 (a) Schematic crystal structure of Mn_6V_{12}; (b) crystal stacking diagram of Mn_6V_{12}; (c) TEM image of Mn_6V_{12}.

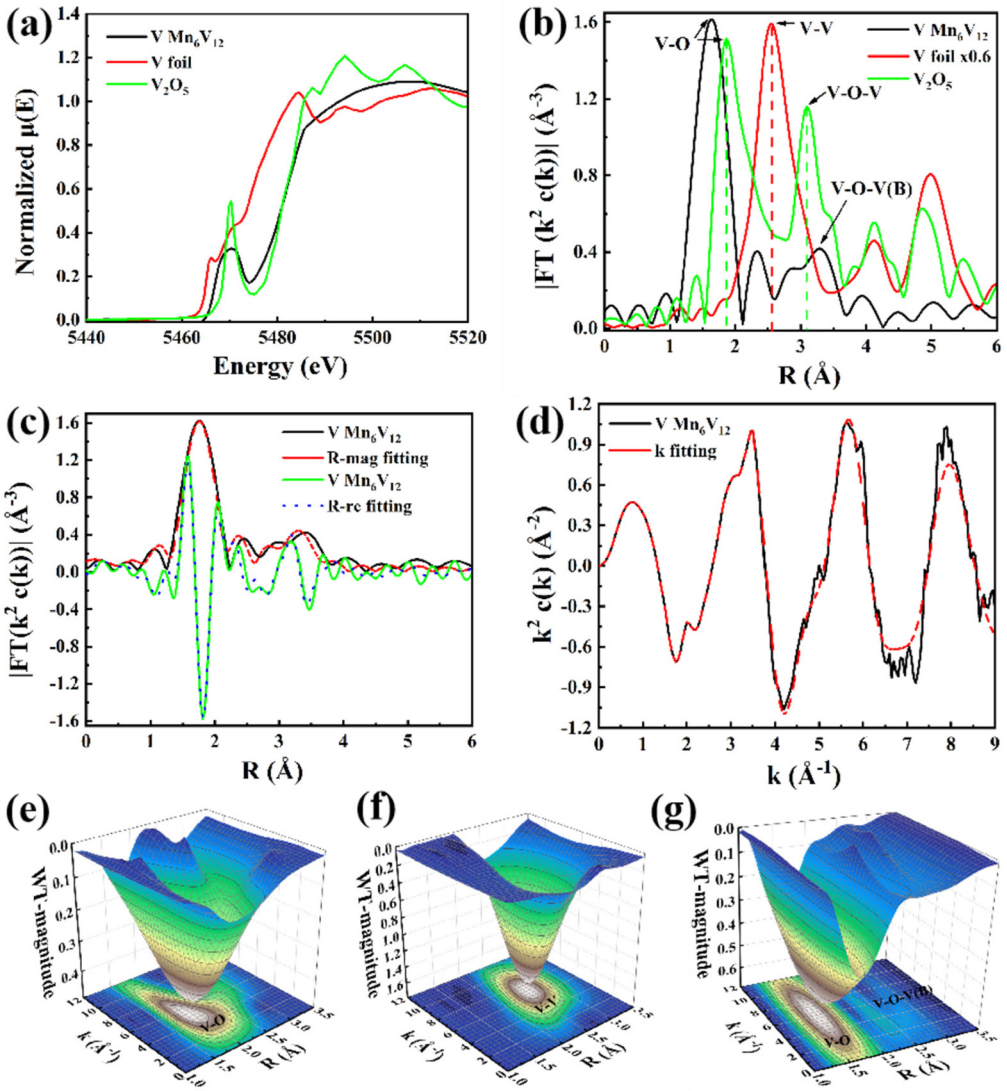

Fig. 2 (a) V K-edge normalized XANES spectra, (b) FT curves of V K-edge EXAFS spectra, (c) V K-edge EXAFS curve fitting at *R* space and *q* space, (d) V K-edge EXAFS curve fitting at *k* space, (e) wavelet transform EXAFS of V_2O_5. (f) Wavelet transform EXAFS of V foil, (g) wavelet transform EXAFS of Mn_6V_{12}.

(XANES) show that the absorption edge of Mn_6V_{12} is located between the absorption edges of V foil and V_2O_5. Mn_6V_{12} exhibits a V K-edge spectrum similar to that of V_2O_5, but the binding energy at the absorption edge of the V K-edge spectrum of Mn_6V_{12} is lower than that of V_2O_5, thus determining that the valence state of V is close to +5 and lower than +5. The leading edge peak at ~5470 eV in Fig. 2a is attributed to the dipole-prohibited 1s to 3d electron jumps,[43] the decrease in the intensity of the leading edge peaks compared to V_2O_5 indicates that the introduction of Mn atoms has resulted in an elevated local symmetry of Mn_6V_{12}. It is shown that Mn_6V_{12} is structurally stable around the V atom. The k2-weighted Fourier transform EXAFS (FT-EXAFS) spectra (after phase correction) of standard V foil, V_2O_5 and Mn_6V_{12} are shown in Fig. 2b. The corresponding specific fitting curves are shown in Fig. 2c and d, and the specific fitting parameters for Mn_6V_{12} on the V k-side are shown in Table S1.† The absence of metal V–V scattering paths (2.55 Å) in the V k-edge EXAFS spectrum of Mn_6V_{12} verifies the atomic dispersion of V (Fig. 2b). The first peak of Mn_6V_{12} is located at 1.63 Å, which is 0.24 Å shorter compared to the representative V–O coordination in V_2O_5 (1.87 Å). The peak of Mn_6V_{12} located at ~3.30 Å is in the vicinity of the V–O–V of V_2O_5 (3.10 Å), which is broad and asymmetric, suggesting the presence of double coordination of V–O–V and V–O–B in Mn_6V_{12}, and in this way, further suggesting that due to the simultaneous presence of the two coordinating sites, there is a shortening of the V–O bond. The optimized model fitted well to the EXAFS spectra (Fig. 2c–d, and Table S1†), and the best-fit analysis clearly confirmed that the coordination numbers of V–O, V–O–B, and V–O–V were 5, 4, and 2, respectively. This means that the V center is connected to 5 O atoms, two of the V atoms are connected by 1 O atom

and the other 2 oxygen atoms are each connected to a B atom, a result that is consistent with the structure of the material. The wavelet transform (WT) (Fig. 2e–g) was applied to the k_2-weighted EXAFS data to further investigate the local environment of V on Mn_6V_{12}. As shown in Fig. 2g, two peaks exist for Mn_6V_{12} at 1.5 Å–1.75 Å and 2.25 Å–2.5 Å, corresponding to V–O and V–O–V(B). Compared to the WT data for V_2O_5 (Fig. 2e), the V–O coordination in Mn_6V_{12} is significantly shortened, consistent with the results in Fig. 2b. In addition, there is no V–V coordination in Mn_6V_{12} compared to V foil (Fig. 2f), further illustrating the atomic dispersion of the V.

From the Mn K-edge X-ray absorption near edge structure (XANES) in Fig. 3a, it can be seen that the absorption edge of Mn_6V_{12} is intermediate between and close to Mn foil and MnO_2, which indicates that the valence state of Mn in Mn_6V_{12} is close to +4. The formation of Mn–N(O) and Mn–N(O)–C(B) coordination in Mn_6V_{12} was directly confirmed by phase-corrected Fourier transform (FT) extended X-ray absorption fine structure (EXAFS) characterization (Fig. 3b). The first peak in the MnO standard sample is located at 2.0 Å and belongs to the Mn–O coordination. Therefore, the main peak at 2.02 Å in the FT-EXAFS spectrum of Mn_6V_{12} can be attributed to the Mn–N[44,45] or Mn–O double coordination environments. The second peak in the Mn_6V_{12} material is located at 3.10 Å, which is 0.15 Å longer compared to Mn–O–Mn (2.95 Å) in MnO, and can be considered as the scattering path of Mn–N(O)–C(B) in the higher shell. It is noteworthy that the Mn–Mn scattering path (2.6 Å) does not exist in this material, verifying the atomic dispersion of Mn.

A quantitative EXAFS curve-fitting analysis of the structural parameters of Mn_6V_{12} was carried out, and the best-fit analysis clearly confirms that the coordination numbers of Mn–N and Mn–N–C, and Mn–O–B are 4, 4, and 1, respectively, which implies that the Mn center is coordinated to four N atoms and one O atom, in accordance with the material structure (Fig. 3c and d; Table S1†). In contrast to Mn foil, MnPC, and MnO_2

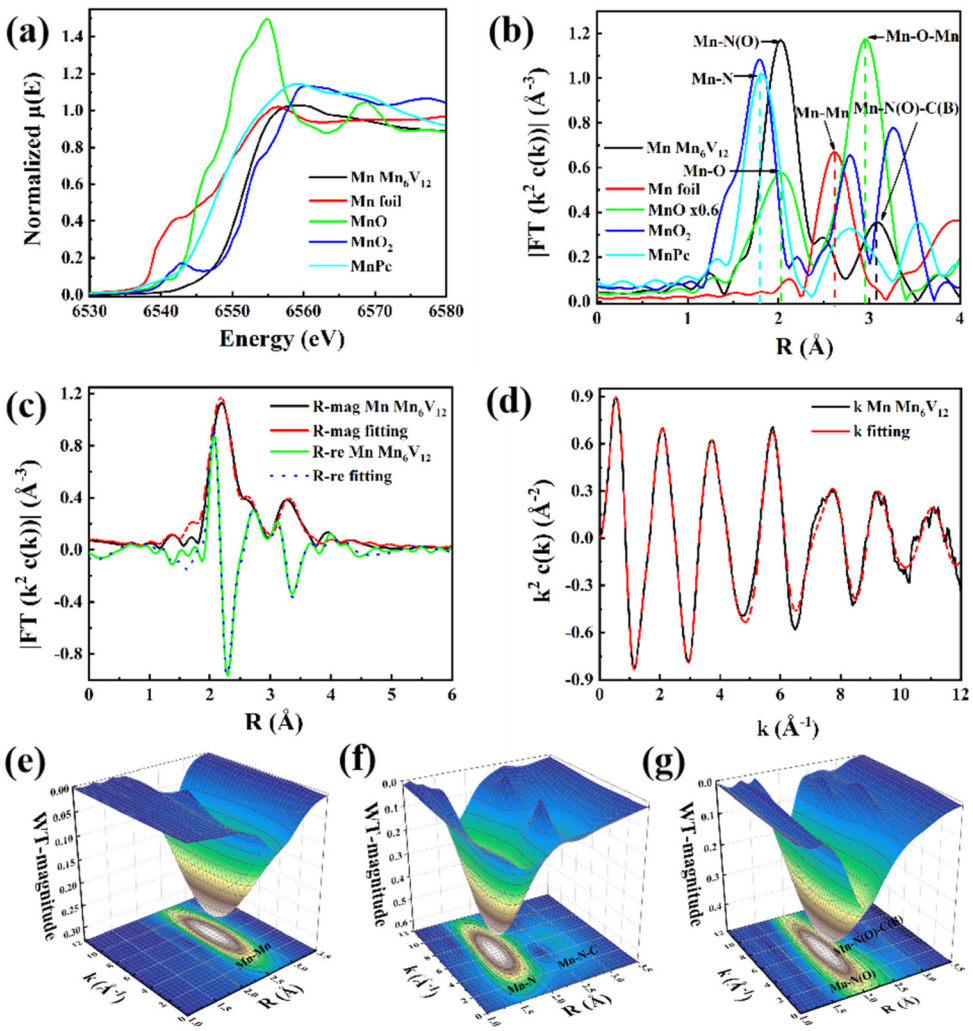

Fig. 3 (a) Mn K-edge normalized XANES spectra, (b) FT curves of Mn K-edge EXAFS spectra, (c) Mn K-edge EXAFS curve fitting at *R* space and *q* space, (d) Mn K-edge EXAFS curve fitting at *k* space, (e) wavelet transform EXAFS of Mn foil, (f) wavelet transform EXAFS of MnPC, (g) wavelet transform EXAFS of Mn_6V_{12}.

shown in Fig. 3e–g, the wavelet transform (WT) results indicate the absence of Mn–Mn bonds (with a maximum bond value (K) of 7 $Å^{-1}$), as well as the presence of Mn–N(O) and Mn–N(O)–C(B) bonds (with a maximum bond value (K) of 5.94 $Å^{-1}$, 6.0 $Å^{-1}$) in this material. This result is consistent with the coordination environment exhibited in Fig. 3b and further illustrates the atomic dispersion of Mn.

Furthermore, the catalyst Mn_6V_{12} was characterized by Fourier transform infrared (FTIR) spectroscopy in the range of 4000–500 cm^{-1}. As shown in Fig. 4a, it is the characteristic peak of V–O bond in the range of 700–1000 cm^{-1}. The strong peaks at 873, 811, and 701 cm^{-1} are due to the antisymmetric stretching vibration peaks of V–O–V (O is the bridging oxygen), and the peak at 945 cm^{-1} is the characteristic peak of V–O (O is the end-group oxygen). The peak at S3–1045 cm^{-1} belongs to the B–O antisymmetric stretching vibration peak belonging to the triangular coordination in the $[B_3O_7]$ unit, and the peak at 1060–1104 cm^{-1} belongs to the B–O antisymmetric stretching vibration peak belonging to the tetrahedral coordination in the $[B_3O_7]$ unit.[46] The appearance of the characteristic peak at 2920 cm^{-1} is a result of symmetric and asymmetric stretching of the C–H bond. The stretching vibrations of N–H have distinct peaks at 1611–1635 cm^{-1} and 3394–3470 cm^{-1}.[47] The characteristic peaks in the infrared spectra of the catalyst before and after the reaction were basically unchanged, indicating that the catalyst structure was relatively stable.

In order to further explore the thermal stability of Mn_6V_{12}, thermogravimetric analyses (TGA) were carried out in N_2 atmosphere in the temperature range from room temperature to 800°C. As shown in Fig. 4b, the TGA curve shows that the mass loss of Mn_6V_{12} is about 8% at 0–800°C, which is due to the decomposition of some free water molecules in the crystals, while the ligand does not collapse and decompose. Therefore, it can be assumed that Mn_6V_{12} can be stabilized at least up to 800°C. For the polyoxometalate photocatalysts $[Co(en)_2]_6[V_{12}B_{18}O_{54}(OH)_6]$ and $[Ni(en)_2]_6[V_{12}B_{18}O_{54}(OH)_6]$, which were also modified with metals, the thermal stability was classified as 200°C and 300°C.[39] Therefore, the thermal stability of the polyoxometalate photocatalyst modified with metal Mn is better.

3.2. Photoreduction of CO_2

The photocatalytic potential of Mn_6V_{12} can be assessed based on the Mn_6V_{12} UV-vis diffuse reflectance spectra (Fig. 4c). Probably due to the effective charge migration between the metal Mn and the ligand, the catalyst exhibited a very broad absorption band in the range of 200 nm to 700 nm, indicating that the catalyst possesses a good light absorption capacity. Meanwhile, the band gap (E_g) of the catalyst was estimated to be 1.76 eV by the Tauc plot method (Fig. 4d), which strongly suggests that Mn_6V_{12} has the potential to be a photo catalyst.

Mott–Schottky measurements under visible light irradiation show that the Mn_6V_{12} flat band potential is −1.50 eV with respect to Ag/AgCl (Fig. 4e), suggesting that Mn_6V_{12} is an n-type semiconductor. For n-type semiconductors, the position of the conduction band (CB) is 0.1 eV lower than the position

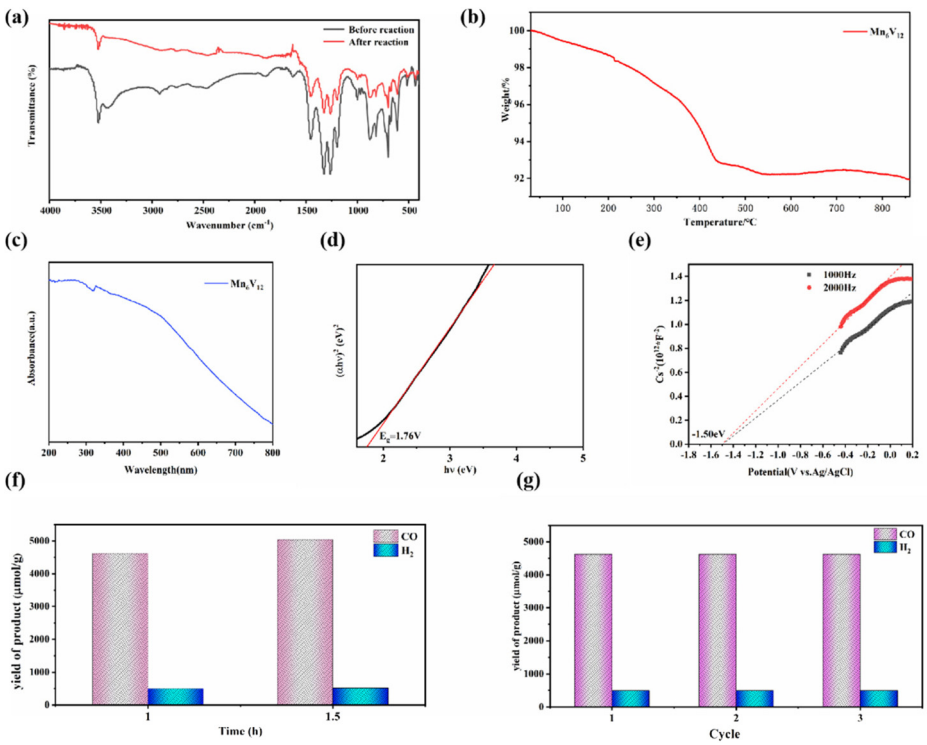

Fig. 4 (a) IR spectra of Mn_6V_{12}; (b) TGA plot of Mn_6V_{12}; (c) UV-visible diffuse reflectance spectra of Mn_6V_{12}; (d) $(\alpha h\nu)^2$ *vs.* $h\nu$ curve of Mn_6V_{12}; (e) the Mott–Schottky plot of Mn_6V_{12} in 0.2 M Na_2SO_4 aqueous solution; (f) gas yield diagram of Mn_6V_{12} in photocatalytic system; (g) stability experiment of Mn_6V_{12} in the same catalytic system.

of the flat band, which is −0.77 eV with respect to Ag/AgCl. According to the equation "(E(*vs.* RHE) = E(*vs.* Ag/AgCl) + 0.197 V + 0.0591 × pH)", the conduction band (CB) of Mn_6V_{12} is −0.77 eV *vs.* RHE. The position of the Mn_6V_{12} conduction band (CB) is more negative than the potential for the reduction of CO_2 to CO (−0.51 eV *vs.* RHE, pH = 7), suggesting that photo excited electrons can be transferred from the catalyst to the CO_2 molecule. The valence band (VB) is 0.99 eV calculated by the equation $E_g + E_{CB} = E_{VB}$.

In the photocatalytic CO_2 reduction system, Mn_6V_{12} was used as a photocatalyst, 2 mL of triethanolamine (TEOA) was used as a sacrificial reagent, 11.6 mg of $[Ru(bpy)_3]$ $Cl_2{\cdot}6H_2O$ was used as a photosensitizer, and 8 mL of acetonitrile (CH_3CN) and 2 mL of deionized water were used as solvents. Comparison test experiments were done to determine the source of the gaseous product CO. When photo catalysis was carried out for 1 h without passing CO_2 gas but other catalytic reaction conditions were not changed, the yield of CO was found to be only 183 μmol g^{-1}, whereas photo catalysis carried out with CO_2 gas resulted in a higher yield of the product CO, which indicated that the carbon source of photo catalysis came from the passed CO_2, rather than acetonitrile (CH_3CN) and triethanolamine (TEOA) in the catalytic system. As shown in Fig. 4f, after 60 min of light exposure, a large amount of CO was detected, and the production of H_2 was detected to be much smaller than that of CO. The production rates of CO and H_2 were 4625.0 μmol g^{-1} and 499.6 μmol g^{-1} respectively, and the production rates of CO and H_2 were 5048.1 μmol g^{-1} and 520.0 μmol g^{-1} respectively, after the light exposure was continued for 30 min. With increasing light time, the yields of CO and H_2 increased successively. The yield of H_2 was much lower than that of CO, implying that the adsorption energy of H_2O on Mn ions and the high free energy of hydrogen precipitation could greatly inhibit the competing precipitation reaction. Comparing the product production rates at 1 h and 1.5 h, it was found that the rate of CO production was 3365.4 μmol g^{-1} h^{-1} and the rate of H_2 production was 346.7 μmol g^{-1} h^{-1} for 1.5 h of light. The rate of product generation was higher for 1 h of light, with 4625.0 μmol g^{-1} h^{-1} for CO and 499.6 μmol g^{-1} h^{-1} for H_2. The selectivity for CO generation was 90.3%, and that for H_2 generation was 9.7%. Fig. S1† displays the CO and H_2 yield in the long reaction time of the Mn_6V_{12}, showing a gradually increased trend. However, the output of the yield per 0.5 h is steadily decreased with time, which can be attributed to the consumption of the photosensitizer agent. In addition, the same type of photocatalysts $[Co(en)_2]_6[V_{12}B_{18}O_{54}(OH)_6]$ and $[Ni(en)_2]_6[V_{12}B_{18}O_{54}(OH)_6]$, after three hours of catalysis required in a similar catalytic system $[Co(en)_2]_6[V_{12}B_{18}O_{54}(OH)_6]$ was catalyzed at a rate of 5700 μmol g^{-1} h^{-1} for CO and 3800 μmol g^{-1} h^{-1} for H_2. $[Ni(en)_2]_6[V_{12}B_{18}O_{54}(OH)_6]$ has a CO production rate of 3200 μmol g^{-1} h^{-1} and H_2 production rate of 300 μmol g^{-1} h^{-1}. By comparison, it was found that polyoxometalate catalyst modified with metal Mn could achieve efficient reduction of CO_2 to CO in this photocatalytic system with only one hour of catalysis and could greatly inhibit the competitive hydrogen evolution reaction (HER). The performance of the Mn modified polyoxometalate photocatalyst was superior to that of the Co and Ni modified polyoxometalate photocatalysts. Moreover, a comparison with the previously reported photocatalysts for this purpose in similar systems (Table S2†) reveals that Mn_6V_{12} exhibits comparatively better performance than other photocatalysts.

Control experiments were conducted to ensure the credibility of the experimental results (Fig. S2†). No observable products including CO and H_2 were detected in the absence of either light or photocatalysts, indicating that both light and photocatalysts are crucial for photocatalytic CO_2 reduction in this system.[48] Almost no product was detected in the absence of the Ru photosensitizer, suggesting that the photogenerated electrons came from Ru photosensitization. Removing TEOA from the system leaded to a conspicuous decline of catalytic activity, because it consumes the photogenerated holes and lessens the recombination rate of photogenerated carriers.[49] Furthermore, when pure CO_2 was not introduced to the reactor, a notable drop of the amount of the products were detected, manifesting the carbon source of CO comes from CO_2.

In addition, in order to test the stability of the photocatalyst, the catalyst was photo catalyzed for 1 h under the same conditions, and the results after repeating the test three times showed a small difference, with no significant change in yield observed (Fig. 4g). This indicates that the catalyst has stable catalytic activity and can efficiently reduce CO_2 to CO and effectively inhibit hydrogen precipitation.

3.3. Photocatalytic mechanism

According to the experimental results, the energy levels of Mn_6V_{12} at the highly occupied molecular orbital (HOMO) and the least occupied molecular orbital (LUMO) are −0.77 eV and 0.99 eV, respectively, with respect to RHE. The energy levels of $[Ru(bpy)_3]$ Cl_2 at the high occupied molecular orbital (HOMO) and lowest occupied molecular orbital (LUMO) are 1.24 eV and −1.25 eV, respectively. Since the E_{CB} value of Mn_6V_{12} is −0.77 eV (*vs.* RHE) lower than the LUMO energy level of $[Ru(bpy)_3]$ Cl_2, electrons on $[Ru(bpy)_3]$ Cl_2 are preferentially transferred to Mn_6V_{12}. In addition, the S_{BET} of Mn_6V_{12} is higher than that of $[Co(en)_2]_6[V_{12}B_{18}O_{54}(OH)_6]{\cdot}17H_2O$ (Fig. S3, S4 and Table S3†), suggesting Mn_6V_{12} may promote CO_2 reduction to CO and restrain the HER process, compared to $[Co(en)_2]_6[V_{12}B_{18}O_{54}(OH)_6]{\cdot}17H_2O$. Furthermore, the Mn_6V_{12} exhibits higher photocurrent and lower interfacial charge transfer resistance than that of $[Co(en)_2]_6[V_{12}B_{18}O_{54}(OH)_6]{\cdot}17H_2O$ (Fig. S5 and S6†), suggesting higher charge separation and transfer efficiency of Mn_6V_{12}, which directly influences the photocatalytic activity for CO_2 reduction.

The possible mechanism of photocatalytic CO_2 reduction to CO and H_2 is that there are two photoelectron transfers in the photocatalytic process. The photosensitizer reaches its excited state under the irradiation of UV-visible light and receives electrons from the triethanolamine electron donor to form the intermediate in the reduced state, while the intermediate in

the reduced state then absorbs the visible light electrons to reach its excited state, and after that it transfers its electrons to the manganese metal ions on the POMs framework, which get the electrons to carry out a reduction reaction on the CO_2 to achieve the photocatalytic reduction of CO_2 to generate CO and H_2. Moreover, according to the results of N_2 adsorption–desorption test, a larger BET surface area of Mn_6V_{12} may promote CO_2 reduction to CO and restrain the HER process.[50] Furthermore, combined with the measurements of photocurrent response and electrochemical impedance spectroscopy, a higher charge separation and transfer efficiency of Mn_6V_{12}, which directly influences the photocatalytic activity for CO_2 reduction, thus leading to more CO production.[51]

4. Conclusions

Polyoxometalate photocatalyst ($[Mn(en)_2]_6[V_{12}B_{18}O_{54}(OH)_6]$) ($Mn_6V_{12}$) with Mn as the modifying unit were synthesized by hydrothermal method, and the highest production rate of CO for catalytic CO_2 reduction was 4625.0 μmol g^{-1} h^{-1}, and the highest production rate of H_2 was 499.6 μmol g^{-1} h^{-1}. The selectivity of CO production was 90.3% and that of H_2 production was 9.7%. This polyoxometalate photocatalyst is good for efficient reduction of CO as well as effective inhibition of hydrogen precipitation reaction. The electronic structure and atomic coordination were elucidated using X-ray absorption near edge structure (XANES) spectroscopy and extended X-ray absorption fine structure (EXAFS) spectroscopy. The study in this work provides new ideas and possibilities for future transition metal modified polyoxometalate for photocatalytic carbon dioxide reduction.

Conflicts of interest

There are no conflicts to declare.

Acknowledgements

We gratefully acknowledge BL17B beamline of National Facility for Protein Science (NFPS), Shanghai Synchrotron Radiation Facility (SSRF) Shanghai, China for providing the beam time. The financial support by “Grassland Talents” of Inner Mongolia Autonomous Region; Young Talents of Science and Technology in Universities of Inner Mongolia Autonomous Region (NJYT23030); “Steed plan High level Talents” of Inner Mongolia University; Carbon Neutralization Research Project (STZX202218); National Natural Science Foundation of China (U22A20107); Inner Mongolia Autonomous Region Natural Science Foundation (2023MS02002); Guangdong Provincial Key Laboratory of Materials and Technologies for Energy Conversion (MATEC2024KF011); National Key R&D Program of China (2022YFA1205201).

References

1 A. Rosas-Hernández, C. Steinlechner, H. Junge and M. Beller, *Green Chem.*, 2017, **19**, 2356–2360.
2 S. You, S. Guo, X. Zhao, M. Sun, C. Sun, Z. Su and X. Wang, *Dalton Trans.*, 2019, **48**, 14115–14121.
3 H. L. Zheng, S. L. Huang, M. B. Luo, Q. Wei, E. X. Chen, L. He and Q. Lin, *Angew. Chem.*, 2020, **132**, 23794–23798.
4 A. A. Dubale, Y. Y. Zheng, H. L. Wang, R. Hübner, Y. Li, J. Yang, J. W. Zhang, N. K. Sethi, L. Q. He, Z. K. Zheng and W. Liu, *Angew. Chem., Int. Ed.*, 2020, **59**, 13891–13899.
5 M. Ding, R. W. Flaig, H.-L. Jiang and O. M. Yaghi, *Chem. Soc. Rev.*, 2019, **48**, 2783–2828.
6 L. R. Dou, L. D. Sun, W. Lyu, M. Y. Wang, F. Gao, M. Gao and H. Jiang, *Pet. Explor. Dev.*, 2023, **50**, 1246–1260.
7 G. Huang, Q. Niu, Y. He, J. Tian, M. Gao, C. Li, N. An, J. Bi and J. Zhang, *Nano Res.*, 2022, **15**, 8001–8009.
8 L. Wang, L. Wang, S. Yuan, L. Song, H. Ren, Y. Xu, M. He, Y. Zhang, H. Wang and Y. Huang, *Appl. Catal., B*, 2023, **322**, 122097.
9 Y. Benseghir, A. Lemarchand, M. Duguet, P. Mialane, M. Gomez-Mingot, C. Roch-Marchal, T. Pino, M.-H. Ha-Thi, M. Haouas and M. Fontecave, *J. Am. Chem. Soc.*, 2020, **142**, 9428–9438.
10 V. R. Calderone, N. R. Shiju, D. Curulla-Ferré, S. Chambrey, A. Khodakov, A. Rose, J. Thiessen, A. Jess and G. Rothenberg, *Angew. Chem., Int. Ed.*, 2013, **52**, 4397–4401.
11 H. X. Zhang, Q. L. Hong, J. Li, F. Wang, X. Huang, S. Chen, W. Tu, D. Yu, R. Xu and T. Zhou, *Angew. Chem., Int. Ed.*, 2019, **58**, 11752–11756.
12 Y.-C. Qiu, S. Yuan, X.-X. Li, D.-Y. Du, C. Wang, J.-S. Qin, H. F. Drake, Y.-Q. Lan, L. Jiang and H.-C. Zhou, *J. Am. Chem. Soc.*, 2019, **141**, 13841–13848.
13 J. Zhou, W. Chen, C. Sun, L. Han, C. Qin, M. Chen, X. Wang, E. Wang and Z. Su, *ACS Appl. Mater. Interfaces*, 2017, **9**, 11689–11695.
14 M. Jiang, Y. Gao, Z. Wang and Z. Ding, *Appl. Catal., B*, 2016, **198**, 180–188.
15 X. Lin, Y. Gao, M. Jiang, Y. Zhang, Y. Hou, W. Dai, S. Wang and Z. Ding, *Appl. Catal., B*, 2018, **224**, 1009–1016.
16 B. Su, M. Zheng, W. Lin, X. F. Lu, D. Luan, S. Wang and X. W. Lou, *Adv. Energy Mater.*, 2023, **13**, 2203290.
17 G. Chen, Z. Zhou, B. Li, X. Lin, C. Yang, Y. Fang, W. Lin, Y. Hou, G. Zhang and S. Wang, *J. Environ. Sci.*, 2024, **140**, 103–112.
18 H. Rao, L. C. Schmidt, J. Bonin and M. Robert, *Nature*, 2017, **548**, 74–77.
19 J. F. Hull, Y. Himeda, W.-H. Wang, B. Hashiguchi, R. Periana, D. J. Szalda, J. T. Muckerman and E. Fujita, *Nat. Chem.*, 2012, **4**, 383–388.
20 Y. Richardson, J. Blin and A. Julbe, *Prog. Energy Combust. Sci.*, 2012, **38**, 765–781.
21 N. Scarlat, J.-F. Dallemand and F. Fahl, *Renewable Energy*, 2018, **129**, 457–472.
22 J. Zhou, H. Wu, C.-Y. Sun, C.-Y. Hu, X.-L. Wang, Z.-H. Kang and Z.-M. Su, *J. Mater. Chem. A*, 2018, **6**, 21596–21604.

23 J. Zhang, Y. Huang, G. Li and Y. Wei, *Coord. Chem. Rev.*, 2019, **378**, 395–414.
24 Z.-J. Liu, X.-L. Wang, C. Qin, Z.-M. Zhang, Y.-G. Li, W.-L. Chen and E.-B. Wang, *Coord. Chem. Rev.*, 2016, **313**, 94–110.
25 J. J. Walsh, A. M. Bond, R. J. Forster and T. E. Keyes, *Coord. Chem. Rev.*, 2016, **306**, 217–234.
26 S.-S. Wang and G.-Y. Yang, *Chem. Rev.*, 2015, **115**, 4893–4962.
27 Z.-Y. Du, Z. Chen, R.-K. Kang, Y.-M. Han, J. Ding, J.-P. Cao, W. Jiang, M. Fang, H. Mei and Y. Xu, *Inorg. Chem.*, 2020, **59**, 12876–12883.
28 H. Zhang, W. Liu, A. Li, D. Zhang, X. Li, F. Zhai, L. Chen, L. Chen, Y. Wang and S. Wang, *Angew. Chem., Int. Ed.*, 2019, **58**, 16110–16114.
29 M. A. Moussawi, M. Haouas, S. Floquet, W. E. Shepard, P. A. Abramov, M. N. Sokolov, V. P. Fedin, S. Cordier, A. Ponchel and E. Monflier, *J. Am. Chem. Soc.*, 2017, **139**, 14376–14379.
30 Z. Wu, Y. Zhai, W. Zhao, Z. Wei, H. Yu, S. Han and Y. Wei, *Green Chem.*, 2020, **22**, 737–741.
31 B. N. Li, X. J. Yu, H. J. Pang, Q. B. Shen, Y. Hou, J. Ma and H. Y. Xin, *Chem. Commun.*, 2020, **56**, 7199–7202.
32 S. Li, S. Liu, S. Liu, Y. Liu, Q. Tang, Z. Shi, S. Ouyang and J. Ye, *J. Am. Chem. Soc.*, 2012, **134**, 19716–19721.
33 W. Zhang, K. Xie, Y. H. Tang, C. Qin, S. Cheng and Y. Ma, *Prog. Chem.*, 2022, **34**, 2638–2650.
34 N. Lu, Y. Wang, S. Ning, W. Zhao, M. Qian, Y. Ma, J. Wang, L. Fan, J. Guan and X. Yuan, *Sci. Rep.*, 2017, **7**, 17298.
35 Y. Qi, J. Zhang, Y. Kong, Y. Zhao, S. Chen, D. Li, W. Liu, Y. Chen, T. Xie, J. Cui, C. Li, K. Domen and F. Zhang, *Nat. Commun.*, 2022, **13**, 484.
36 X. Liu, J. Zhou, T. R. Amarante, F. A. Almeida Paz and L. Fu, *Dalton Trans.*, 2021, **50**, 1550–1568.
37 H. Chen, Z. B. Yu, Z. Bacsik, H. Zhao, Q. Yao and J. Sun, *Angew. Chem., Int. Ed.*, 2014, **53**, 3608–3611.
38 J. T. Rijssenbeek, D. J. Rose, R. C. Haushalter and J. Zubieta, *Angew. Chem., Int. Ed.*, 2003, **36**, 1008–1010.
39 X. Yu, C.-C. Zhao, J.-X. Gu, C.-Y. Sun, H.-Y. Zheng, L.-K. Yan, M. Sun, X.-L. Wang and Z.-M. Su, *Inorg. Chem.*, 2021, **60**, 7364–7371.
40 P. Hermosilla-Ibáñez, K. Wrighton-Araneda, L. Scarpetta-Pizo, W. Cañón-Mancisidor, M. Gutierrez-Cutiño, E. Le Fur, V. Paredes-García and D. Venegas-Yazigi, *New J. Chem.*, 2019, **43**, 17538–17547.
41 C. Liu, Y. Wu, K. Sun, J. Fang, A. Huang, Y. Pan, W.-C. Cheong, Z. Zhuang, Z. Zhuang and Q. Yuan, *Chem. Commun.*, 2021, **7**, 1297–1307.
42 Z. Cai, P. Wang, J. Zhang, A. Chen, J. Zhang, Y. Yan and X. Wang, *Adv. Mater.*, 2022, **34**, 2110696.
43 K. Zhu, S. Wei, H. Shou, F. Shen, S. Chen, P. Zhang, C. Wang, Y. Cao, X. Guo, M. Luo, H. Zhang, B. Ye, X. Wu, L. He and L. Song, *Nat. Commun.*, 2021, **12**, 6878.
44 L. Lai, H. Ji, H. Zhang, R. Liu, C. Zhou, W. Liu, Z. Ao, N. Li, C. Liu, G. Yao and B. Lai, *Appl. Catal., B*, 2021, **282**, 119559.
45 D. Zhao, X. Wang, W. Zhang, Y. Zhang, Y. Lei, X. Huang, Q. Zhu and J. Liu, *Adv. Funct. Mater.*, 2023, 2211412.
46 Z. H. Lin, H. H. Zhang, C. C. Huang, R. Q. Sun, Y. P. Chen and X. Y. Wu, *Acta Chim. Sin.*, 2004, **62**, 391–398.
47 S. Li, B. Feng, X. Zhang, J. Tian, D. Wang, Y. Pei, M. Qiao, Y. Li and B. Zong, *Appl. Catal., B*, 2023, **335**, 122879.
48 S. Liu, F. Chen, S. Li, X. Peng and Y. Xiong, *Appl. Catal., B*, 2017, **211**, 1–10.
49 Z. Liu, Z. Chen, M. Li, J. Li, W. Zhuang, X. Yang, S. Wu and J. Zhang, *ACS Catal.*, 2023, **13**, 6630–6640.
50 W.-J. Wang, K.-H. Chen, Z.-W. Yang, B.-W. Peng and L.-N. He, *J. Mater. Chem. A*, 2021, **9**, 16699–16705.
51 S. Li, S. Shi, G. Huang, Y. Xiong and S. Liu, *Appl. Surf. Sci.*, 2018, **455**, 1137–1149.